

We are IntechOpen, the world's leading publisher of Open Access books Built by scientists, for scientists

6,900

Open access books available

186,000

International authors and editors

200M

Downloads

Our authors are among the

154

Countries delivered to

TOP 1%

most cited scientists

12.2%

Contributors from top 500 universities



WEB OF SCIENCE™

Selection of our books indexed in the Book Citation Index
in Web of Science™ Core Collection (BKCI)

Interested in publishing with us?
Contact book.department@intechopen.com

Numbers displayed above are based on latest data collected.
For more information visit www.intechopen.com



Nanoscale III-V Semiconductor Photodetectors for High-Speed Optical Communications

Jack Jia-Sheng Huang, Yu-Heng Jan, H.S. Chang,
Chih-Jui Ni, Emin Chou, Shih-Kai Lee,
Horng-Shyang Chen and Jin-Wei Shi

Additional information is available at the end of the chapter

<http://dx.doi.org/10.5772/intechopen.73054>

Abstract

Nanophotonics involves the study of the behavior of light on nanometer scale. Modern nanoscale semiconductor photodetectors are important building blocks for high-speed optical communications. In this chapter, we review the state-of-the-art 2.5G, 10G, and 25G avalanche photodiodes (APDs) that are available in commercial applications. We discuss the key device parameters, including avalanche breakdown voltage, dark current, temperature dependence, bandwidth, and sensitivity. We also present reliability analysis on wear-out degradation and optical/electrical overload stress. We discuss the reliability challenges of nanoscale photodetectors associated with device miniaturization for the future. The reliability aspects in terms of high electric field, Joule heating, and geometry inhomogeneity are highlighted.

Keywords: semiconductor photodetectors, avalanche photodiodes, APD photodetectors, InGaAs/InAlAs APD, III-V photodetectors, nanophotonics, reliability, temperature dependence, device miniaturization

1. Introduction

Recently, two-dimensional (2D) materials have drawn great interest in the field of nanophotonics. The 2D material sometimes is referred to as single-layer material, composed of a single layer of atoms. One notable example of the single-layer material is graphene that was discovered by Nobel Laureates Andre Geim and Konstantin Novoselov in 2004 [1]. Since then, a vast amount of research has been directed at 2D materials because of their novel characteristics and potential use in the applications of photovoltaics, semiconductors, electrodes, and water purification.

Generally, 2D materials can be classified into two categories. The first is called 2D allotrope, a material consisting of single elements. Among them, the most widely studied 2D allotrope is graphene. Graphene is a 2D single-atom-thick material consisting of a monolayer of carbon atoms in a honeycomb array. It exhibits unusual electronic [2] and magnetic [3] properties such as high carrier mobility and ambipolar effect. Graphene is considered as a revolutionary material for future generation of high-speed electronic, radio frequency logic devices, thermally/electrically conductive reinforced composites, sensors, transparent electrodes, and so on [2–6].

The second category is a 2D compound composed of two or more covalently bonding elements [7]. Layered combinations of different 2D materials are generally called van der Waals heterostructures. However, the efficient integration of 2D functional layers with three-dimensional (3D) systems remains a significant challenge, limiting device performance and circuit design.

Since the first discovery of 2D graphene, there have been about 700 2D materials predicted to be stable, and many of them remain to be explored and synthesized [8]. The global market for 2D materials is expected to reach US\$390 million within a decade, mostly for graphene in the semiconductor, electronics, battery energy, and composites markets [9–12].

2. Nanoscale photonic and electronic devices

Although 2D materials exhibit great technological potential, modern commercial photonic and electronic devices are mainly based on 3D nanoscale structures. Several 2D materials such as graphene photodetectors [13] and InAs quantum membranes [14] have been demonstrated in research laboratories with the promising performance. Nevertheless, efficient integration of 2D functional layers with 3D systems remains a significant challenge, hence limiting its commercial use. Moreover, high-volume manufacturing is still immature, and reliability issues remain unknown.

Three-dimensional nanostructures are the main building blocks of modern photonic and electronic components because of their proven technology and established field reliability. **Table 1** lists the smallest feature size of photonic and electronic devices that are commercially fabricated by using 3D nanostructures. For the electronics sector, integrated circuit (IC) has been deployed in vast majority of semiconductor products [15]. In the IC, the feature size refers to the smallest features on an IC where the feature size is usually gated by the length of the transistor channel [16]. Over the past few decades, the IC has followed Moore's law where the number of transistors has roughly doubled in about every 18 months [17–19]. The recent examples of IC's device miniaturization include the 32 nm technology used in Apple's A5/A6 chips for iPad Mini/iPhone 5, the 28 nm technology in Apple's A7 chip for iPad Air, the 20 nm technology in Apple's A8 chip for iPhone 6, the 16 nm technology in Apple's A9/A10 chips for iPhone 6S/iPhone 7, and the 10 nm in A11 chip for iPhone 8 [20, 21].

For the photonics sector, avalanche photodiodes (APDs) have followed similar device scaling with less restrictions in design rule and technology roadmap. The APD structure is typically composed of a thick absorption layer, a charge control layer, and a multiplication layer (M-layer) for avalanche device operation. Among the various layers of APD, the charge control

	Photonic sector: APD photodetector	Electronic sector: IC transistor
Recent technology since 2010	2.5G APD: <ul style="list-style-type: none">• M-layer about 500 nm• Charge control layer~100 nm 10G APD: <ul style="list-style-type: none">• M-layer about 160–200 nm• Charge control layer~50 nm 25G APD: <ul style="list-style-type: none">• M-layer about 80–100 nm• Charge control layer~30 nm	32 nm node: <ul style="list-style-type: none">• Transistor length~32 nm 28 nm node: <ul style="list-style-type: none">• Transistor length~28 nm 20 nm node: <ul style="list-style-type: none">• Transistor length~20 nm 16 nm node: <ul style="list-style-type: none">• Transistor length~16 nm 10 nm node: <ul style="list-style-type: none">• Transistor length~10 nm
Future technology	50G APD: <ul style="list-style-type: none">• M-layer < 80 nm• Charge control layer < 30 nm 100G APD <ul style="list-style-type: none">• M-layer < 50 nm• Charge control layer < 20 nm	7 nm node <ul style="list-style-type: none">• Transistor length~7 nm 5 nm node <ul style="list-style-type: none">• Transistor length~5 nm 3 nm node <ul style="list-style-type: none">• Transistor length~3 nm

Table 1. List of minimum feature size of photonic and electronic devices based on 3D nanostructures. The devices that are commercially fabricated at the present and in the future are shown.

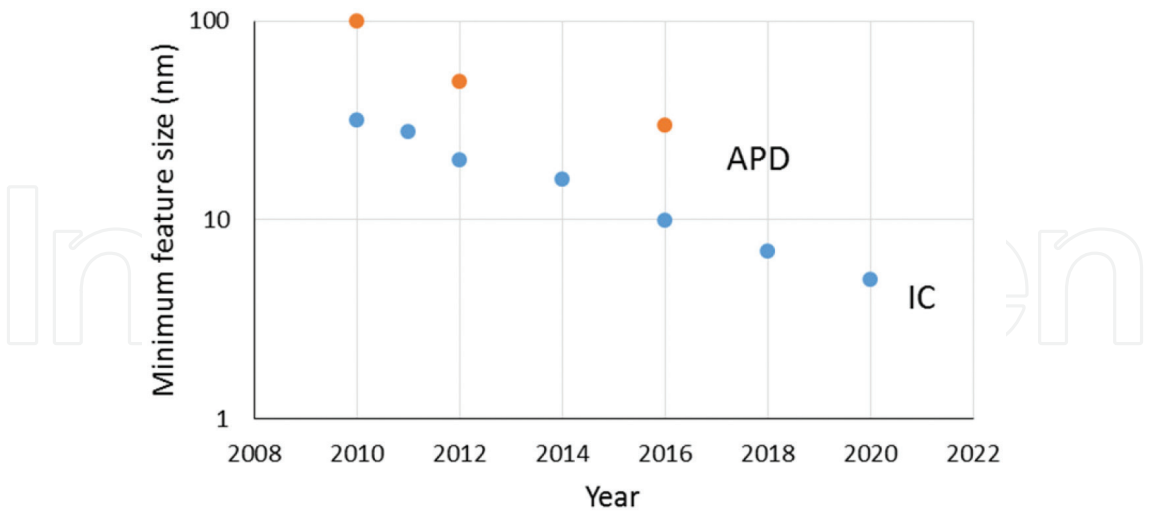


Figure 1. Evolution of minimum feature size for APD and IC. Device miniaturization occurs for both photonic and electronic devices to attain higher speed.

layer is denoted as the minimum feature size. Semiconductor photodetectors have evolved from 2.5G APD to 10G APD and recently advanced to 25G APD [22, 23]. Driven by 100G data-center demand, the development and manufacturing of 25G APD have been accelerated with

rapid pace and growth [24–26]. Comparing the charge control layer, the feature size roughly reduced from about 100 nm in 2.5G APD to 50 nm in 10G APD and continued to shrink to about 30 nm in 25G APD.

Figure 1 shows the evolution of the minimum feature size for photonic and electronic devices where APD and IC are taken as the respective examples of photonics and electronics devices. The year indicates roughly the time of commercial manufacturing. For APD, the charge control layer scales with device speed in a similar fashion compared to IC. For IC, device scaling has rigorously followed Moore’s law for decades.

3. Nanoscale III-V semiconductor photodetectors

Semiconductor photodiodes are important components for high sensitivity, low-noise receivers, and detectors deployed in the optical communication systems such as passive optical network (PON) [27]. Among the photodiode portfolio, APDs are attractive devices due to their significant improvement in photoreceiver sensitivity compared with traditional p-i-n (PIN) photodiodes [28]. By adding the multiplication layer, the avalanche photodiodes combine the detection and amplification properties simultaneously.

Recently, 10G and 25G APDs have drawn great interest in commercial and military applications due to their high bandwidth and low-noise performance advantages. In order to achieve high bandwidth, a mesa structure with coplanar P and N electrodes is typically employed [29–32]. For APD, there are two critical device parameters for the reverse bias operation. The first parameter is the avalanche breakdown voltage associated with the multiplication layer. The breakdown voltage is typically measured at reverse current of 10 μ A. The avalanche breakdown has been formulated to study the impact ionization coefficients of electrons and holes [33–35]. The second parameter is the dark current that is typically measured at reverse bias below the breakdown voltage. Since these two parameters strongly influence the device performance of the APD, it is important to understand the temperature dependence of these two parameters. A good knowledge of temperature dependence is critical for the design of robust APD that can maintain stable performance when subject to temperature fluctuations. In Sections 3.1–3.4, we discuss the avalanche breakdown voltage, dark current, and temperature dependence in detail.

Table 2 summarizes the device cross-sectional schematics and key features of 2.5G APD, 10G APD, and 25G APD. There are several differences between 2.5G APD and 10G/25G APD. First, planar-type design is usually employed in 2.5G APD due to the advantages of processing simplicity and low cost. On the other hand, mesa-type structure has been incorporated in the high-speed APD such as 10G and 25G. Second, the p-InP region of 2.5G APD is typically formed by Zn diffusion in the intrinsic InP layer [35], while the p-InP of 10G and 25G APDs is grown by molecular beam epitaxy (MBE) to attain more precise control [23, 24].

For 2.5G APD, the device shown in Table II is composed of p-InP/i-InP/n-InP/i-InGaAs/n-InP. From top to bottom, the first layer is the p-InP formed by Zn diffusion. Guard ring is formed to avoid the edge breakdown at the p-InP diffused region. The intrinsic InP underneath the p-InP serves as the multiplication layer. Next, a thin layer (\sim 100 nm) of n-type InP

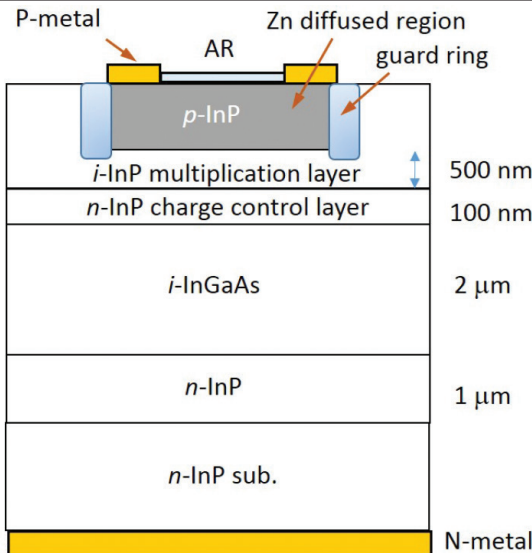
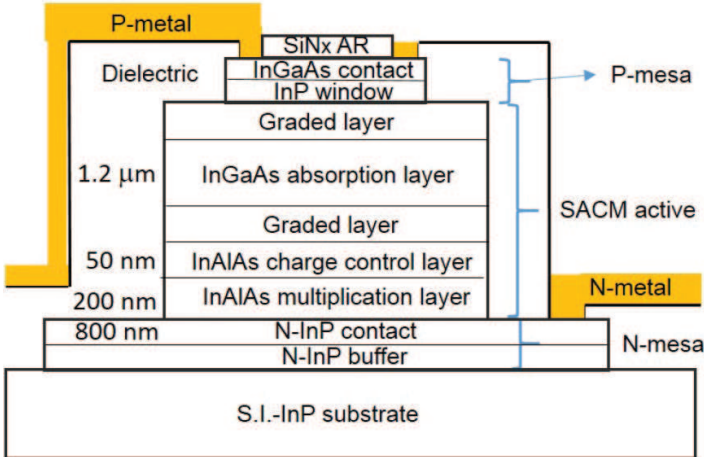
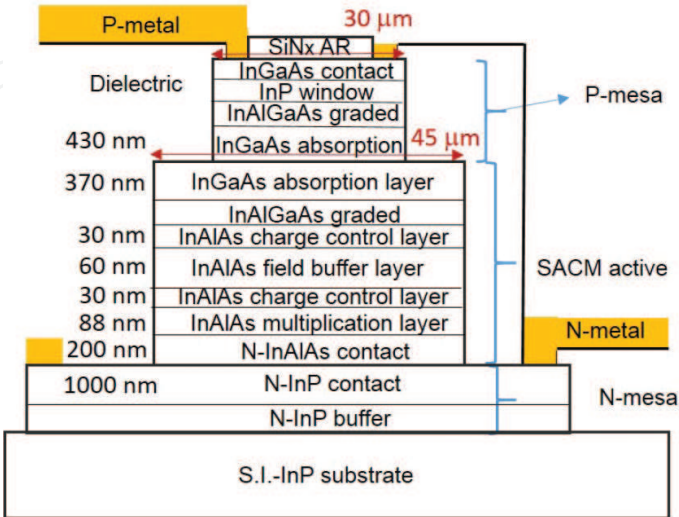
	Device structure	Key feature
2.5G APD		<ul style="list-style-type: none">• Planar-type• Hole carrier for multiplication• InP multiplication layer (~500 nm) determined by Zn diffusion• Charge control layer (~100 nm) by epitaxial growth
10G APD		<ul style="list-style-type: none">• Mesa-type• Electron carrier for multiplication• InAlAs multiplication layer (160–200 nm) grown by MBE• Charge control layer (50 nm) grown by MBE
25G APD		<ul style="list-style-type: none">• Mesa-type• Dual charge layer• Electron carrier for multiplication• InAlAs multiplication layer (80–100 nm) grown by MBE• Charge control layer (30 nm) grown by MBE

Table 2. Structure cross-sectional schematics and key features of 2.5G APD, 10G APD, and 25G APD. The schematics are not drawn in scale [23, 24, 35].

is used as charge control. The intrinsic *i*-InGaAs of 2 μm in thickness is for absorption. Below the *i*-InGaAs, there are n-InP buffer and n-InP substrates.

For 10G APD, mesa-type structure with coplanar p- and n-metal contacts is employed to enhance the speed [23, 36]. The active region is sandwiched between the P-mesa at the top and the N-mesa at the bottom. The P-mesa consists of the p-InP window and p-InGaAs contact layers. The p-contact is usually made by forming a metal ring immediately outside the antireflective (AR) window. The p-ring is connected to the outside p-pad by the metal bridge. The active region consists of the InAlAs multiplication, InAlAs charge control, graded InGaAs/InAlAs, and InGaAs absorption layers. Such active structure is also called separate absorption, charge, and multiplication (SACM). The InGaAs absorption layer is undoped with a thickness of about 1200 nm. The InAlAs charge control layer is p-type doped ($\sim 1.0\text{--}1.1 \times 10^{18} \text{ cm}^{-3}$). The InAlAs multiplication layer is undoped with a thickness of about 160 nm. The N-mesa, consisting of the N-InP buffer and contact layers, is grown on a semi-insulating (S.I.) InP substrate. The n-metal contact is connected to the N-mesa. For the passivation, the low-k dielectric material such as polyimide is used to reduce the capacitance.

For 25G APD, more sophisticated mesa structure such as dual charge layers has been designed to improve the bandwidth-gain product [22, 24]. Table II shows the conceptual cross-sectional views of a top-illuminated 25G APD device structure. The epitaxial layers are grown by molecular beam epitaxy (MBE). From top to down, it is composed of the p⁺-InGaAs contact layer, p⁺-InP window layer, p-type partially depleted InGaAs absorber, two p-type InAlAs charge layers, one intrinsic InAlAs field buffer layer, one intrinsic InAlAs multiplication (M-) layer, and n⁺-InAlAs/InP contact layers. The partially depleted p-type absorber, which has a graded doping profile (top: 5×10^{19} to bottom: $1 \times 10^{17} \text{ cm}^{-3}$) is used to shorten the hole transit time, accelerate the electron diffusion process, and increase the high-power and linearity performances [36]. The total thickness of InGaAs absorber is 0.8 μm and the ratio of depleted versus p-doped region is chosen to balance the RC delay and internal carrier transit/avalanche-delay time under low gain operation ($M_G < 5$) [24]. In order to shorten the avalanche delay time, a thin M-layer (around 90 nm) is chosen in our device structure [22, 36].

3.1. IV characteristics of APD

Figure 2 shows the typical reverse current-voltage (IV) curve of a 10G mesa-type SACM APD photodetector. On IV curve, there are two transitions along the reverse voltage at about 10 and 32 V, respectively. When the reverse voltage is applied to the device, the InAlAs multiplication layer begins to be depleted first. The first transition at 10 V corresponds to the punch-through voltage at which electric field depletes the InAlAs multiplication and *i*-InGaAs absorption layers [23, 37]. The punch-through voltage related to the absorption layer is denoted as V_{pt} . The second transition represents the avalanche breakdown voltage (V_{br}) for APD. The breakdown is typically determined by the InAlAs multiplication layer. By properly controlling the charge density of the charge control layer, sufficient electric field can be reached to achieve a good avalanche gain while keeping the tunneling and impact ionization away from the InGaAs absorption layer. In this case, the breakdown voltage taken at 10 μA is estimated to be 31.7 V. Between the two transitions, the reverse current is of technological importance for optical detection. The dark current is usually referred to the reverse current at 0.9 V_{br} . In this case, the dark current is estimated to be about 12.1 nA at 20°C.

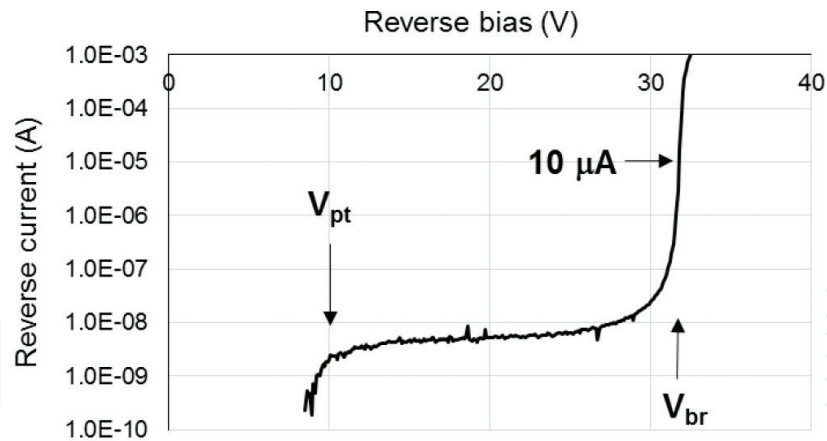


Figure 2. Typical IV characteristics of 10G InAlAs mesa-type APD. The IV is measured in reverse bias at 20°C [23].

Figure 3 shows the typical reverse IV of a 25G mesa-type SACM APD photodetector [38]. On the IV curve, there are two transitions along the reverse voltage that occur at 3 and 26 V, respectively. Again, the first transition at 3 V corresponds to V_{pt} at which the electric field depletes both the InAlAs multiplication and i-InGaAs absorption layers [23]. The second transition represents V_{br} determined by the InAlAs multiplication layer. The avalanche breakdown voltage taken at 10 μ A is estimated to be about 26 V for this device. The typical range of avalanche breakdown voltage is 24–26 V. The dark current refers to the reverse current at 0.9 V_{br} is estimated to be about 13.4 nA at 25°C.

3.2. Avalanche breakdown mechanism

Figure 4 shows the schematic cross-section and the internal electric field profile of a SACM APD [39]. A top illumination is illustrated here where the absorption layer is next to the charge control and multiplication layers.

There are two major types of junction breakdown in semiconductor diodes. The first type is associated with the tunneling breakdown where the tunneling mechanism is dominant for the devices with lower breakdown voltage. The tunneling breakdown process exhibits a negative temperature coefficient [40, 41]. The second is the avalanche breakdown that is the dominant mechanism for large breakdown voltage, as illustrated in **Figure 5**. At very high electric field ($\sim 10^5$ – 10^6 V/cm), some electrons within the diffusion distance near the depletion layer gain enough energy to create the secondary electron-hole pair by raising the electron from the valence band into the conduction band. This excitation process creates an electron-hole pair due to impact ionization. The electrons and holes created by the impact ionization are accelerated by high electric field. Consequently, the secondary electron-hole pair can create even more carriers, leading to a snowball avalanche effect. The avalanche breakdown process typically shows a positive temperature coefficient.

3.3. Temperature dependence

Figure 6 shows the reverse IV as a function of temperature for the mesa-type APD. The breakdown of APD is due to the avalanche mechanism since the device is operating at high electric field. At higher temperature, the avalanche breakdown voltage is expected to increase due to

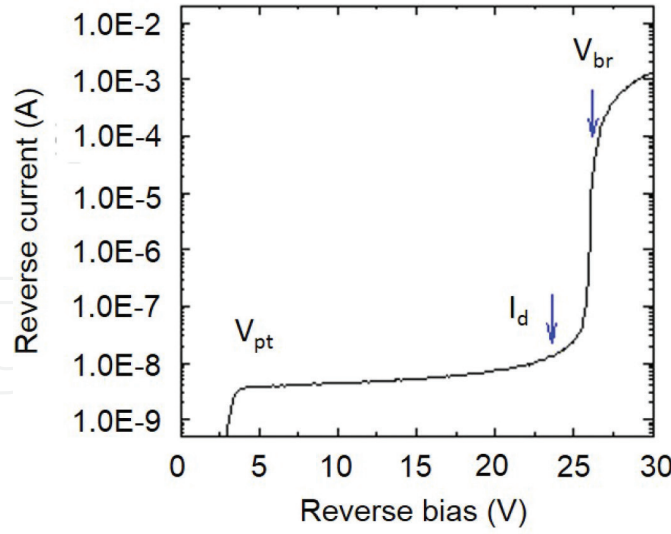


Figure 3. The reverse IV curve of the 25G mesa-type APD photodetector where the first transition is related to the punch-through (V_{pt}) and the second related to the avalanche breakdown (V_{br}) [38].

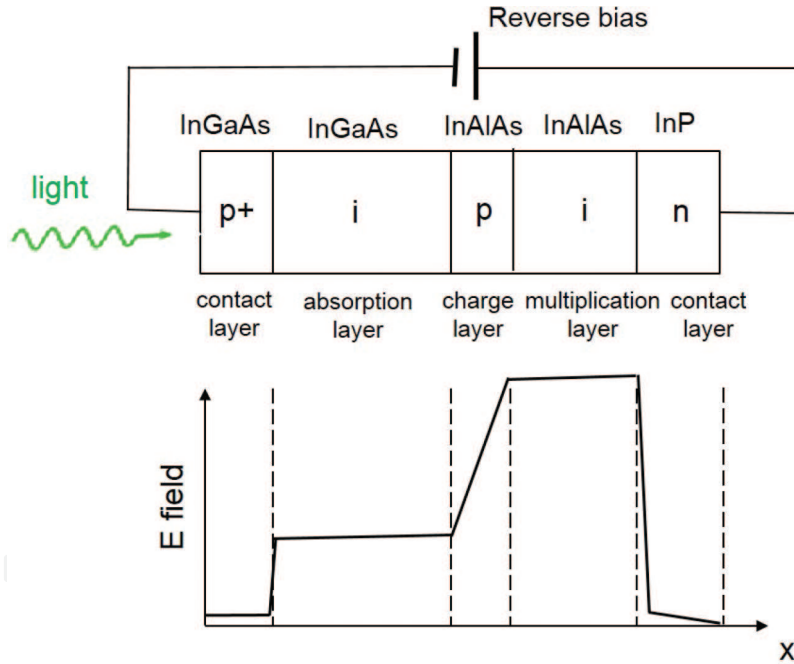


Figure 4. Schematic cross-section and internal electric field profile of the SACM APD structure. In the illustration, the InGaAs absorption layer is next to the InAlAs charge control and multiplication layers [39].

the effect of phonon [42]. As the temperature increases, the population of phonons increases. Thus, a higher electric field and applied voltage are required to reach breakdown in order to overcome the increased carrier cooling caused by phonon scattering [43].

The positive temperature coefficient of the APD has been experimentally found and theoretically described where the breakdown voltage of the Si APD followed a linear expression with temperature [44]. Here, it is assumed that the avalanche breakdown voltage increased linearly with increasing temperature as shown in Eq. (1).

$$V_{br}(T) = V_{br}(T_0)[1 + \alpha(T - T_0)] \quad (1)$$

where $V_{br}(T)$ is the avalanche breakdown voltage at temperature T , $V_{br}(T_0)$ is the avalanche breakdown voltage at reference temperature T_0 , and α is the normalized temperature coefficient. For the sake of comparison, Eq. (1) can be rewritten as Eq. (2) where the second term shows the temperature coefficient of the breakdown voltage.

$$V_{br}(T) = V_{br}(T_0) + \alpha V_{br}(T_0)(T - T_0) \quad (2)$$

Figure 7 shows the avalanche breakdown voltage as a function of temperature based on two APD wafers with similar structures but from different processing runs. There are several

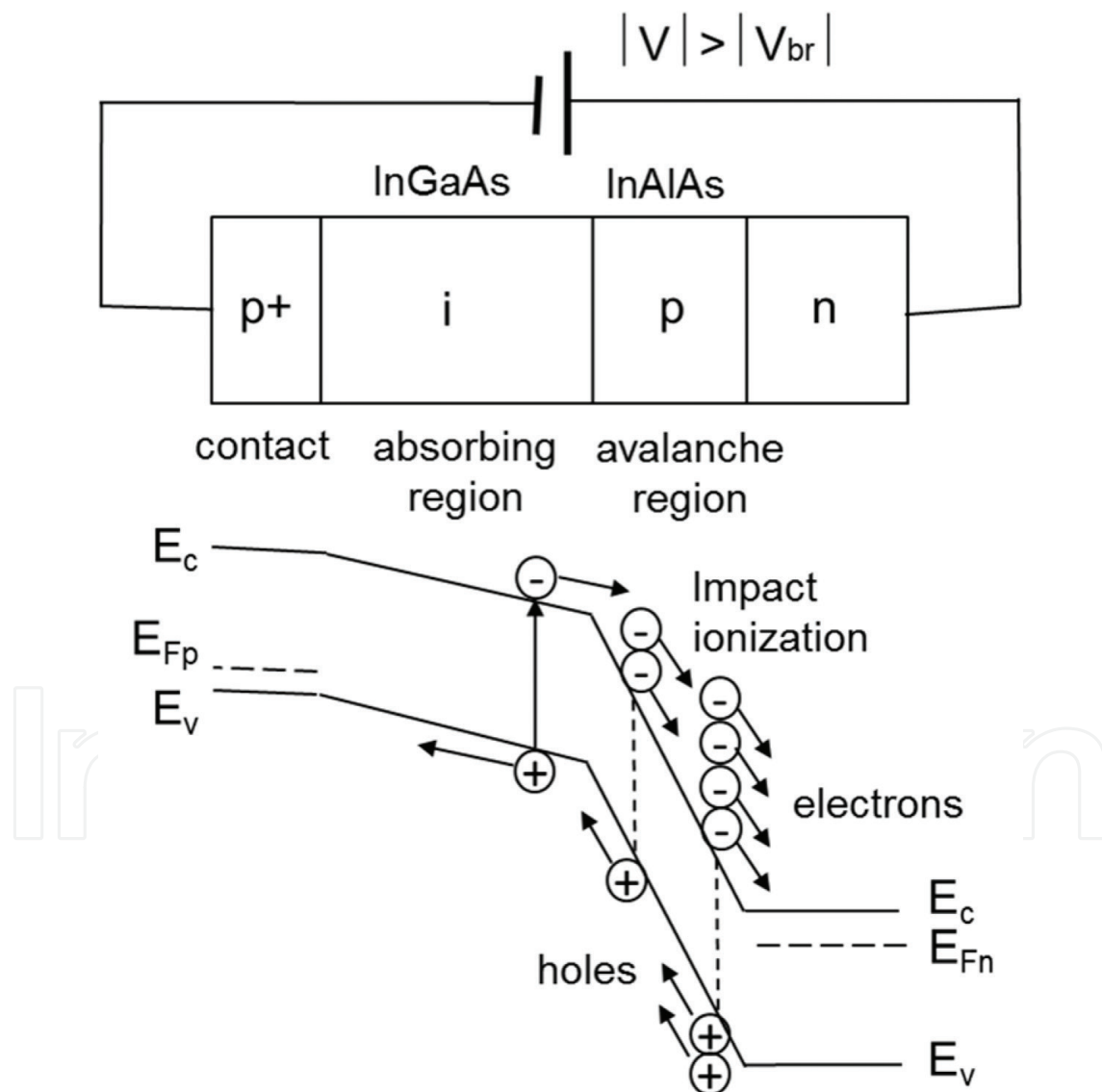


Figure 5. Schematics of avalanche breakdown mechanism of APD with simplified energy band diagram at the reverse voltage of $|V| > |V_{br}|$. The electron with high enough kinetic energy drifts to the avalanche region and gets accelerated to create a secondary electron-hole pair. The secondary electron-hole pair in turn generates another electron-hole pair, leading to snowball avalanche process [23].

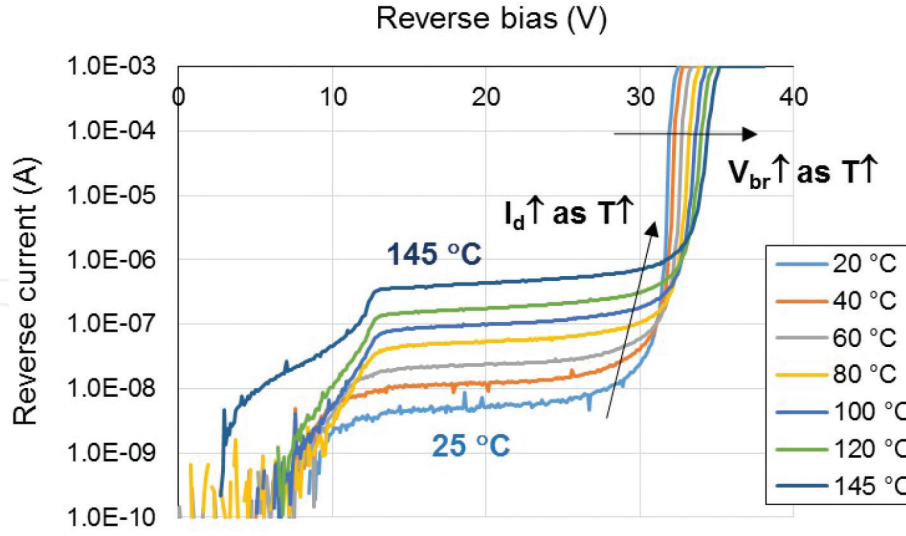


Figure 6. The reverse IV of 10G mesa-type APD as a function of temperature over a wide range of 20–145°C [23].

interesting features worth mentioning. First, the two wafers show similar breakdown voltage. The intercepts at the reference temperature ($T_0 = 20^\circ\text{C}$) for wafers A and B are 32.8 and 31.7 V, respectively. The similarity between the wafers from two different processing runs suggests that the breakdown voltage is largely determined by the epitaxial structure. Second, both wafers show the same temperature coefficient of breakdown voltage where αV_{br} taken from the slope in **Figure 6** is equal to $0.017 \text{ V}/^\circ\text{C}$. Third, the normalized temperature coefficient α is determined to be 5.1×10^{-4} and $5.5 \times 10^{-4} \text{ }^\circ\text{C}^{-1}$, as shown in **Table 3**. The measured value of the normalized temperature coefficient in the mesa-type APD is excellent, lower than the reported value of $7.2 \times 10^{-4} \text{ }^\circ\text{C}^{-1}$ [45]. The superior temperature dependence of our mesa-type InGaAs/InAlAs APD can bring performance advantage to maintain the gain when the device is subject to temperature fluctuations. The superior temperature dependence of the avalanche

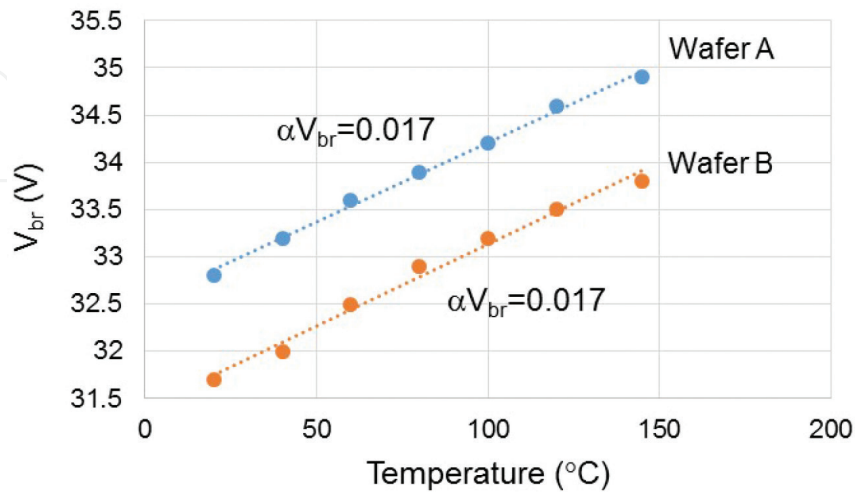


Figure 7. The breakdown voltage of mesa-type APD as a function of temperature from 20 to 145°C. The symbols are experimental data, and the dashed lines are fitting from Eq. (2) [23].

	$V_{br}(T_0)$	$\alpha V_{br}(T_0)$	α
Wafer A	32.8 V	0.017 V/°C	$5.1 \times 10^{-4} / ^\circ\text{C}$
Wafer B	31.7 V	0.017 V/°C	$5.5 \times 10^{-4} / ^\circ\text{C}$

Table 3. The temperature dependence of the mesa-type APD measured from 20 to 145°C [23].

breakdown voltage can be attributed to the optimized design of the InAlAs multiplication layer thickness and InAlAs charge control layer doping.

3.4. Dark current, I_d

Another key device parameter of APD is dark current [46, 47]. As shown in **Figure 6**, the dark current is typically referred to the reverse current below the breakdown voltage. For different temperature ranging from 20 to 145°C, the dark current is taken from the reverse voltage of $0.9 V_{br}$ where V_{br} increases with the temperature. **Figure 8** illustrates the transport

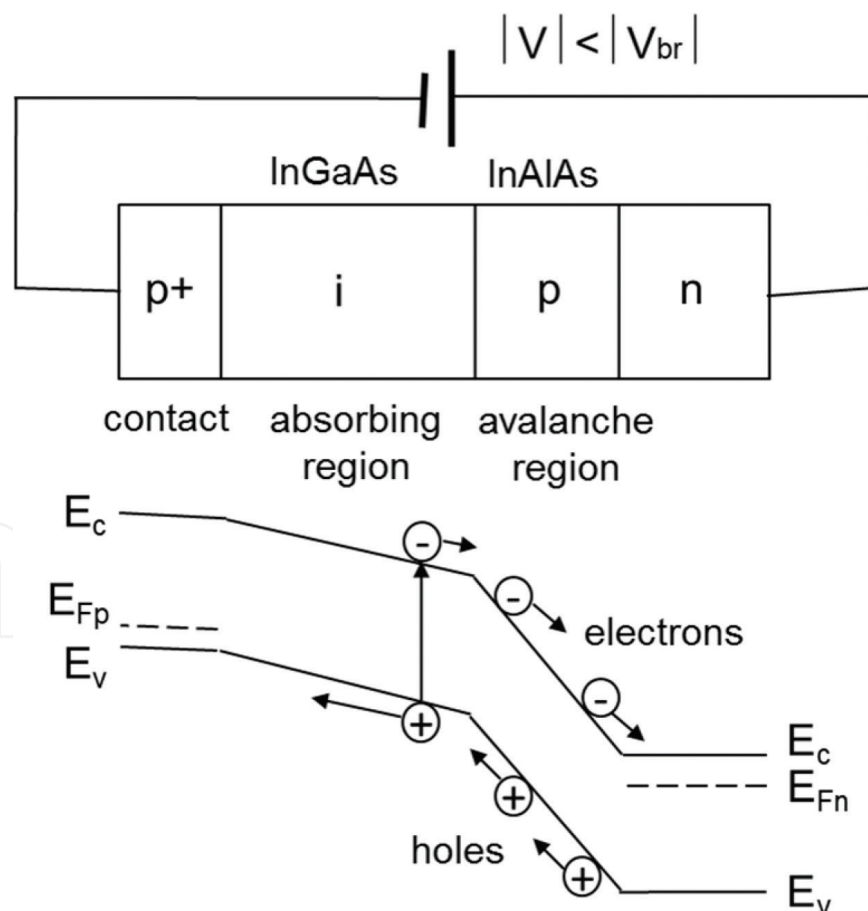


Figure 8. Schematics of reverse depletion mechanism of APD with simplified energy band diagram at the reverse voltage of $|V| < |V_{br}|$. The avalanche process is not operative below V_{br} . At $10 < |V| < |V_{br}|$, both *i*-InGaAs absorption and InAlAs multiplication layers are depleted [23].

of electrons and holes in the energy diagram at the reverse voltage below the avalanche breakdown ($|V| < |V_{br}|$) and above the punch-through voltage ($|V| > 10$). In this regime, both *i*-InGaAs absorption and InAlAs multiplication layers are depleted, but the avalanche breakdown in the multiplication layer is not activated.

It has been found that the dark current increases with increasing temperature due to the influence of bandgap energy [48]. We note that the generation-recombination component of the dark current has temperature dependence. Therefore, the bandgap could be estimated based on the temperature dependence of the dark current. The generation current can be expressed in Eq. (3) where A_{pn} is the area of the p-n junction, W is the width of the depletion region, q is the carrier charge, σ is the carrier capture cross-section, v_{th} is the carrier thermal velocity, N_t is the trap density, and n_i is the intrinsic carrier concentration.

$$I_{dg} = A_{pn} W q \sigma v_{th} N_t n_i \quad (3)$$

The intrinsic carrier concentration can be expanded in Eq. (4) where N_c is the effective density of state in the conduction band, N_v is the effective density of state in the valence band, $E_g(T)$ is the energy bandgap, k is the Boltzmann's constant, and T is the temperature. The energy bandgap, $E_g(T)$, shows a temperature dependence where the bandgap value decreases with increasing temperature [49].

$$I_{dg} = A_{pn} W q \sigma v_{th} N_t (N_c N_v)^{1/2} \exp\left(-\frac{E_g(T)}{2kT}\right) \quad (4)$$

Based on Eq. (4), the energy bandgap can be extracted from the plot of dark current versus temperature. Taking the natural logarithm of Eq. (4), the temperature dependence of the dark current can be expressed in Eq. (5). The slope in the plot of I_d versus $1/kT$ shown in **Figure 9** is equal to $-E_g(T)/2$. The energy bandgap is estimated to be about 0.71 eV, close to the value of InGaAs where the bandgap energy of $\text{In}_{0.53}\text{Ga}_{0.47}\text{As}$ is reported to be 0.75 eV at 295 K [50, 51]. The slight difference between our value and others is likely attributable to the variance from junction temperature and test measurement.

$$\ln(I_d) \sim \left(-\frac{E_g(T)}{2}\right) \left(\frac{1}{kT}\right) \quad (5)$$

3.5. Bandwidth

Figure 10 shows the bandwidth plot of a 25G APD based on small-signal modulation response at 25°C. The bandwidth curves measured at reverse voltage of -17 and -21 V are shown. At the reverse bias of -17 V, the bandwidth taken by the 3 dB roll-off can reach 20 GHz. Such bandwidth is adequate for meeting the requirement of $4 \times 25\text{G ER4}$ Ethernet [24]. The corresponding multiplication factor or gain at -17 V is about 2.2 ($M = 2.2$). As the reverse bias was adjusted to -21 V for high gain operation ($M = 5$), the 3 dB bandwidth can be maintained at around 15 GHz.

3.6. Sensitivity

Figure 11 shows the bit error rate (BER) of a 25G APD photodetector as a function of input optical power. At the reverse bias near V_{br} , the 25G APD can achieve error-free bit error

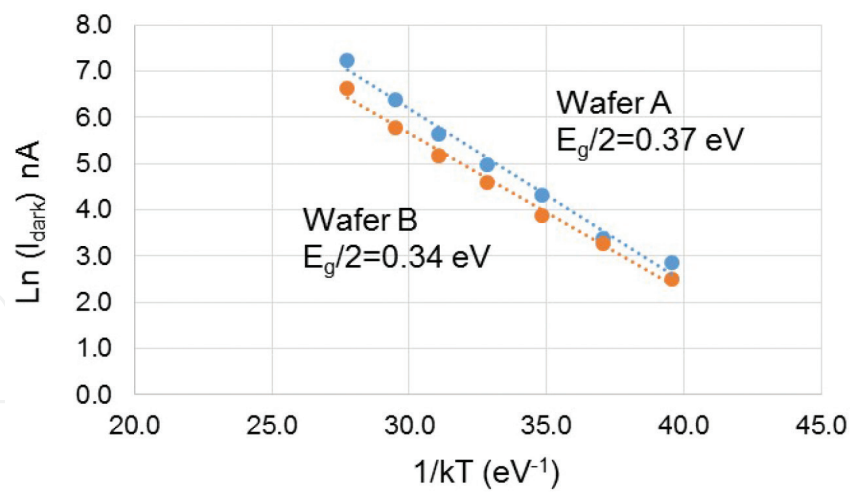


Figure 9. The natural logarithm of dark current versus reciprocal of temperature for mesa-type APD. The dark current was measured from 20 to 145°C [23].

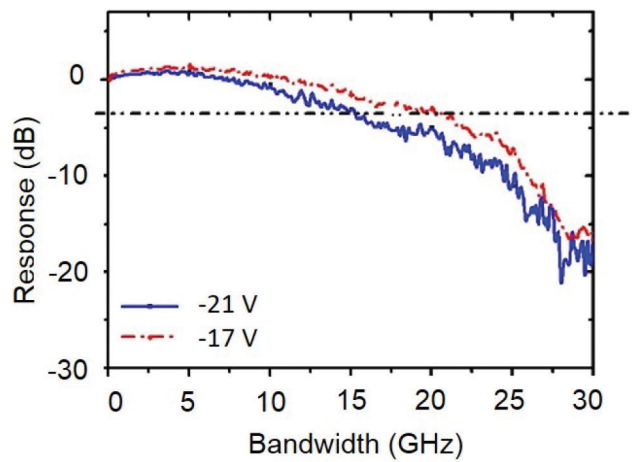


Figure 10. Bandwidth plot of 25G APD photodetector measured at 25°C with the reverse bias at -17 and -21 V. For a gain of 2, the BW can reach 20 GHz [38].

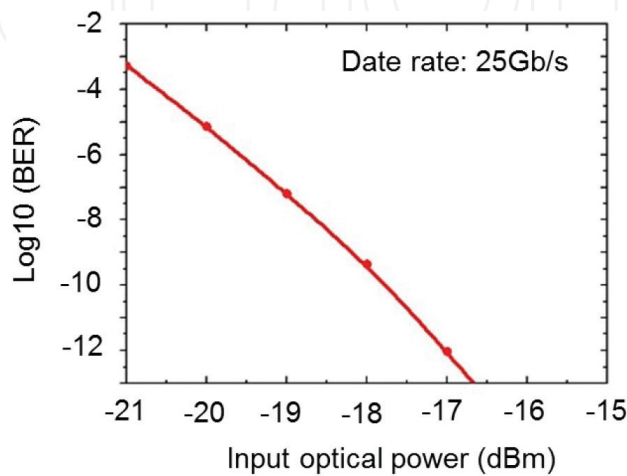


Figure 11. BER of a 25G APD device showing that the sensitivity of -17 dBm can be achieved for BER of 10^{-12} [38].

rate (BER) < 10⁻¹² and the sensitivity of -17 dBm with a gain of 6. Such sensitivity level can provide a good margin for photoreceiver detection over the 40 km transmission over fiber [52, 53].

4. Reliability

4.1. Optical and electrical overload stress

In order to verify photodetector’s robustness against the simultaneous electrical and optical stresses, fiber optic component manufacturers typically perform overload stress in burst and continuous modes, as illustrated in **Figure 12**. To determine the damage threshold of overload, optical stress is ramped up from -4 to +4 dBm when APD is subjected to electrical stress at $V_{br} - 2$ V.

In the burst mode, the optical stress of 1% pulsed duty cycle is applied to the APD for 60 s. With robust design and process, the APD devices can achieve good survival rate under the harsh overload stress. **Table 4** summarizes the overload results indicating that no failure occurs after being overload stressed up to +4 dBm. In the continuous mode, the damage threshold can also sustain the stress level of +1 dBm, well exceeding the requirement for -6 dBm.

For the study of reliability physics, it is important to identify the failure location and morphology of APD device after the overload stress. **Figure 13** shows an example of the damage morphology of the mesa-type APD sample stressed with an overload test of +4 dBm at burst mode. After the stress, the APD device shows functional failure due to short circuit, likely related to the InAlAs window. The short failure can be correlated with the metal shorting that shunts between the top InGaAs contact layer and the InAlAs multiplication layer, punching through

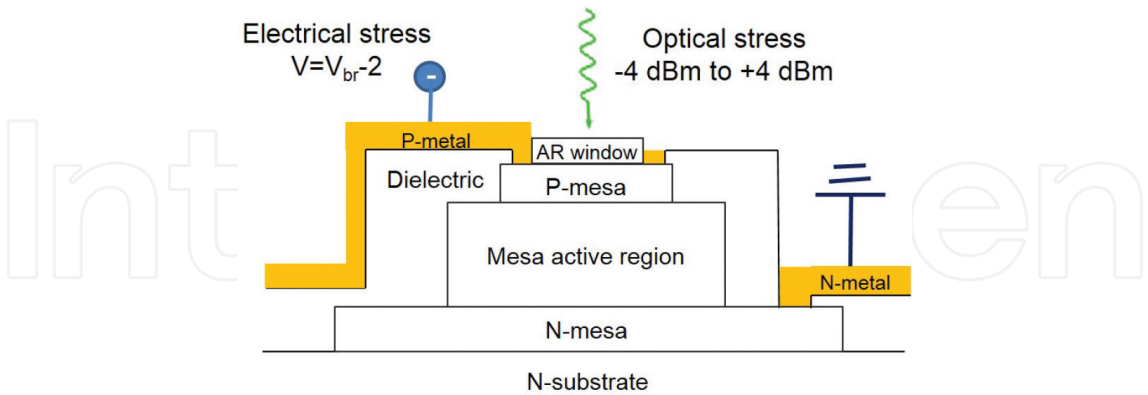


Figure 12. Schematic of electrical and optical overload stress applied to the APD for both burst and CW modes [38].

	Burst mode	CW mode
Damage threshold	No failure up to +4 dBm	No failure up to +1 dBm

Table 4. Damage threshold of optical and electrical overload stresses of 25G APD for burst and CW modes [38].

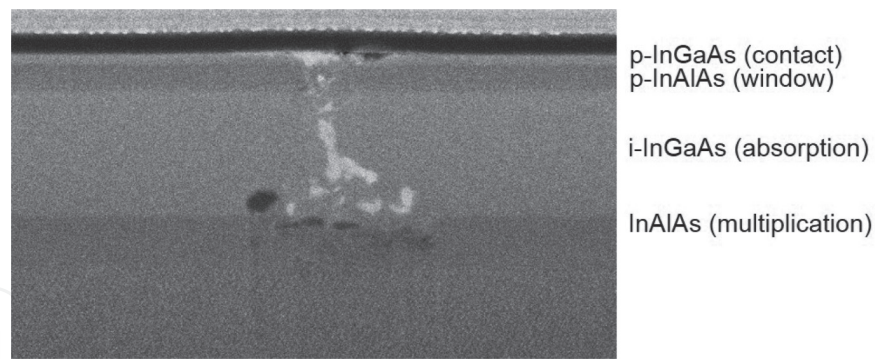


Figure 13. Failure morphology of a damaged mesa-type APD device after electrical and optical overload stress.

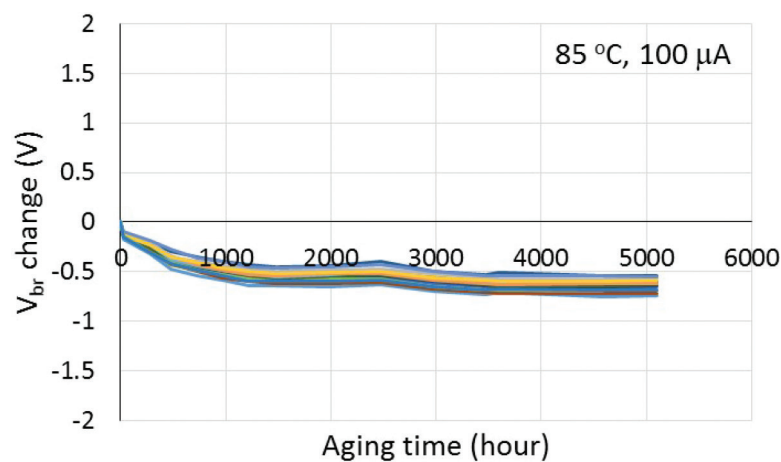


Figure 14. The relative breakdown voltage change as a function of aging time based on the stress condition of 85°C, 100 μ A [38].

the InGaAs absorption layer. In comparison, the short failure can be suppressed by employing an InP window structure. The failure morphology reveals the spatial location of the weak spot and provides useful information about the robust overload design for the photodetector.

4.2. Reliability aging data

To establish long-term reliability performance, the APD devices are tested with temperature and current stresses to monitor the degradation. [54]. **Figure 14** shows the relative change in avalanche breakdown voltage as a function of aging time where the mesa-type APD samples are stressed at 85°C under a reverse current of 100 μ A. The failure criterion is defined as 1 V change in V_{br} . All APD photodetectors pass reliability test with excellent reliability margin after 5100 h aging.

Due to the small degradation at regular aging condition of 85°C, mesa-type APD devices are also stressed at highly elevated temperature experimentally determine the failure times. **Figure 15** shows the failure time distributions of the APD from the aging groups of 165 and 175°C. The failure time at 50% cumulative probability shows the statistical mean-time-to-failure (MTTF). The MTTF values for 165 and 175°C are 896 and 446 h, respectively.

The device failure time (t_f) follows the modified Black’s Eq. [55–57] which provides a good empirical description of device degradation over time as a function of stress current and temperature as shown in Eq. (6).

$$t_f = \frac{A}{I^N} \exp\left(\frac{E_a}{kT}\right) \tag{6}$$

In Eq. (6), the first term represents the current acceleration factor where A is a constant, I is the stress current, and N is the current exponent; the second term represents the temperature acceleration where E_a is the activation energy, k is the Boltzmann’s constant, and T is the temperature.

For the sake of activation energy study, Eq. (6) can be rewritten in the form of natural logarithm as shown in Eq. (7) where the third term can readily determine the activation energy.

$$\ln(MTTF) = \ln(A) - N \cdot \ln(I) + \frac{E_a}{kT} \tag{7}$$

Figure 16 shows the plot of $\ln(MTTF)$ versus $1/(kT)$ where the slope is equal to E_a . Based on the experimental aging data of 165 and 175°C, the E_a of APD is estimated to be 1.18 eV, which is in close agreement with other reported values [27, 58].

With the E_a establishment, the failure times from the aging test can be extrapolated to project the device lifetimes at the operating condition by using Eq. (6). For the operating condition of 50°C, the device lifetime of the mesa-type APD is estimated to be around 6900 years as shown in **Table 5**, which represents great reliability margin for the 20 year stringent requirement per Telcordia.

4.3. Future reliability challenges

Nowadays, semiconductor devices often incorporate design-in reliability in the early development phase [21, 59, 60]. During device miniaturization, several aspects including high electric field, Joule heating, and geometry inhomogeneity may impose reliability challenges.

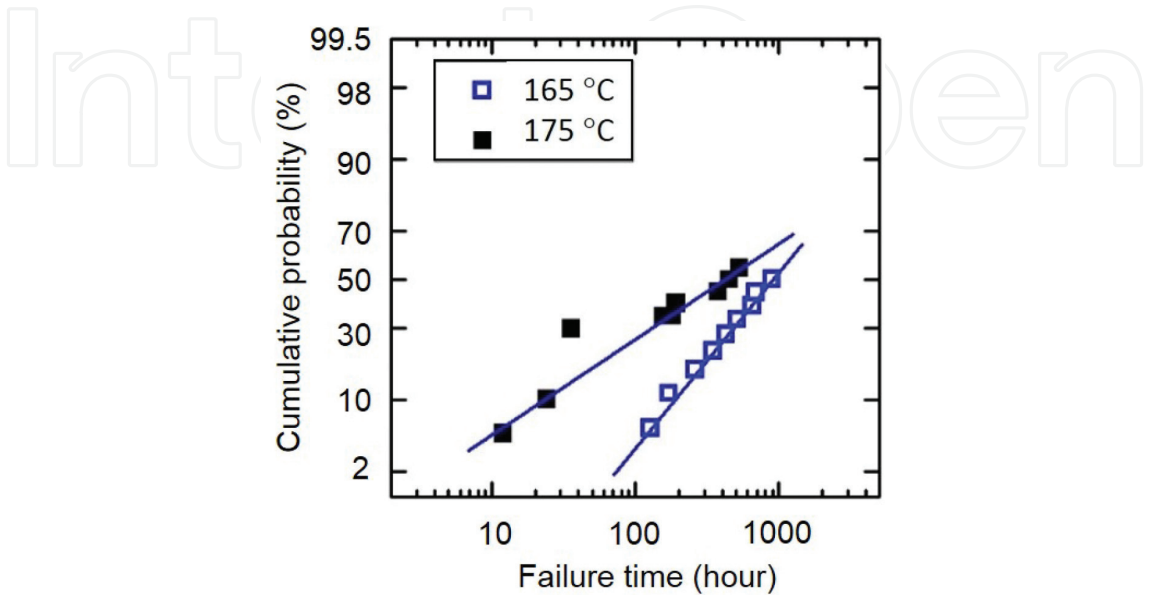


Figure 15. The failure time distributions of APD photodetectors based on the stress condition of 165 and 175°C [38].

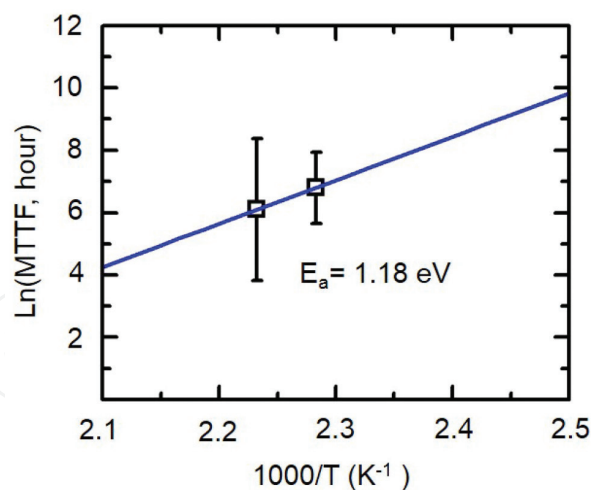


Figure 16. The plot of $\text{Ln}(\text{MTTF})$ versus $1/(kT)$ for the determination of E_a measured by mesa-type APD devices. The E_a value was 1.18 eV [38].

Aging stress temperature	Failure time at stress temperature	Device operating lifetime at 50°C
165°C	896 h	6912 years
175°C	446 h	6909 years

Table 5. Projected device lifetime of mesa-type APD at 50°C operating condition based on extrapolation from the stress condition [38].

(1) High electric field

The breakdown electric field of APD generally increases with decreasing thickness of multiplication layer. The increase in electric field with feature size reduction can accelerate device degradation over long-term field use [61–63].

(2) Joule heating

As device size shrinks, Joule heating is expected to be increased at a given bias current [64–66]. The increased Joule heating would raise device junction temperature that may degrade functional performance and long-term reliability.

(3) Geometry inhomogeneity

For electronic IC, the geometry inhomogeneity may induce current crowding and cause early reliability failure [67–69]. For APD, the inhomogeneous structure is typically generated by mesa etch [70–72]. The etched mesa interface may cause an increase in leakage current due to the generation of surface state [70, 71].

Among the three factors mentioned above, high electric field may impose the most reliability challenge for APD. This is because the effect of Joule heating can be mitigated by the use of mesa-type structure. For example, the resistance of the mesa-type APD is typically lower than that of the planar-type due to the shorter conduction path [73]. The lower resistance would result in lower Joule heating. Regarding geometry inhomogeneity, the surface leakage from mesa structure is expected to be similar from design standpoint. With careful processing control, the dark current of modern mesa-type APD devices can be confined within a few tens of nanoampere [23, 38].

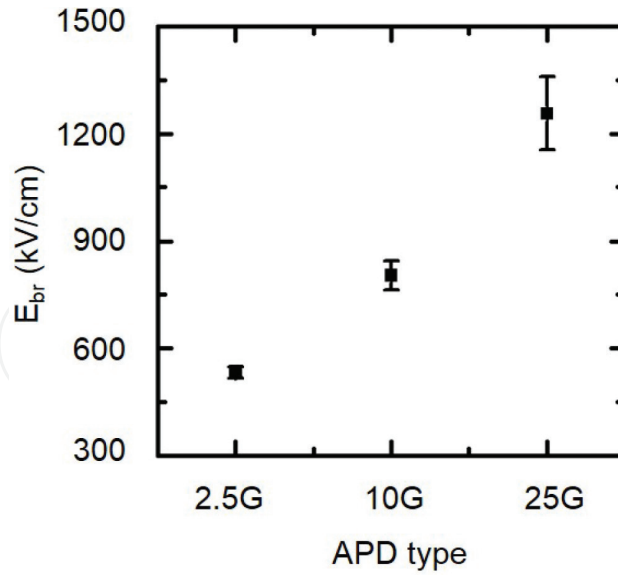


Figure 17. The breakdown electric field of the multiplication layer for various APD generations. Generally, the breakdown field increases with increasing device speed [39].

Figure 17 shows the estimated breakdown electric field in the multiplication layer of commercial 2.5G, 10G, and 25G APDs. At the breakdown voltage for avalanche operation, majority of the voltage drop typically occurs at the absorption layer and multiplication layer [22]. Since the absorption layer is very thick, the electric field of the absorber is usually low enough to prevent breakdown. Due to the thin layer, the electric field is much higher in the multiplication layer as shown in the electric field profile in **Figure 4**. Assuming half of the voltage drop is across the multiplication layer, we can estimate the electric breakdown field at the multiplication layer [74]. It is shown that the breakdown field may reach about 800 and 1300 kV/cm for 10G APD and 25G APD, respectively.

Although the breakdown field depends on the design of epitaxial doping and thickness [38], the ballpark estimate shown in **Figure 17** suggests that reliability issue may need to be extensively studied for 25G APD and beyond. As illustrated in our recent studies [26, 75, 76], the two seemingly different fields of electronics and photonics share some interesting similarities in reliability physics. As device scaling continues to occur to attain higher speed and greater performance, 25G APD and beyond may mark another new frontier of reliability studies. With effort as relentless as IC industry, the reliability robustness of APD is expected to be achieved and matured in the forthcoming.

5. Conclusions

In this chapter, we review the state-of-the-art commercial APD photodetectors. A 2.5G APD is typically based on the planar-type structure where the p-InP is formed by Zn diffusion with guard ring on the edge of diffused region to avoid edge breakdown. The advantages of planar-type APD include processing simplicity and low cost. On the other hand, 10G and 25G APDs are based on more sophisticated mesa-type structures in order to meet the speed requirements. The common mesa-type APD photodetectors are composed of SACM where the absorption, charge control, and multiplication layers are precisely grown and controlled by MBE.

The important device parameters of APD include: (1) avalanche breakdown voltage, (2) dark current, (3) temperature coefficient, (4) bandwidth, and (5) sensitivity.

1. For the avalanche breakdown voltage, the typical V_{br} of 10G and 25G APD photodetectors are about 31 and 26 V, respectively. The V_{br} value may vary depending on the design and process of component vendors.
2. The dark current of modern planar-type and mesa-type APDs is typically in the range of a few tens of nanoampere. By plotting the dark current versus temperature, the activation energy close to the energy bandgap of InGaAs (~ 0.75 eV) can be found.
3. The temperature dependence of avalanche breakdown voltage shows a positive coefficient due to the effect of phonon. The temperature coefficient of the breakdown voltage is determined to be 0.017 V/ $^{\circ}\text{C}$, corresponding to a normalized temperature coefficient of $5.1 \times 10^{-4}^{\circ}\text{C}^{-1}$. The superior temperature dependence of the avalanche breakdown voltage is attributable to the optimized design of the InAlAs multiplication layer thickness and InAlAs charge control doping.
4. The typical 3 dB bandwidths of 10G and 25G APDs can reach around 8 and 20 GHz, respectively. The bandwidth is a function of voltage bias and multiplication gain.
5. The sensitivity and BER are paramount to high-speed photodetection. For the BER of 1×10^{-12} , a sensitivity of -17 dBm or better can be achieved.

The main reliability assessment of APD photodetector includes: (1) life test aging and (2) optical/electrical overload.

1. For the life test aging, mesa-type APDs can pass 5000 h aging with V_{br} change of <0.5 V at the stress condition of 85°C , $100 \mu\text{A}$. Based on the aging data of 165 and 175°C , the activation energy of the APD is estimated to be 1.18 eV. The projected device lifetime of the APD is extrapolated to be about 6900 years at the operating condition of 50°C .
2. For the overload, APD is tested for its durability against simultaneous electrical and optical stresses. In the burst mode, the APD usually shows higher level of optical stress durability with a threshold up to $+4$ dBm. In the CW mode, the damage threshold is around $+1$ dBm, also exceeding the requirement of -6 dBm.

Author details

Jack Jia-Sheng Huang^{1,2*}, Yu-Heng Jan^{1,2}, H.S. Chang², Chih-Jui Ni², Emin Chou², Shih-Kai Lee², Horng-Shyang Chen² and Jin-Wei Shi³

*Address all correspondence to: jack.huang@sourcephotonics.com

1 Source Photonics, West Hills, CA, USA

2 Source Photonics, Hsinchu, Taiwan

3 Department of Electrical Engineering, National Central University, Zhongli, Taiwan

References

- [1] Novoselov KS, Geim AK, Morozov SV, Jiang D, Zhang Y, Dubonos SV, Grigorieva IV, Firsov AA. Electric field effect in atomically thin carbon films. *Science*. 2004;**306**:666-669
- [2] Castro Neto AH, Guinea F, Peres NMR, Novoselov KS, Geim AK. The electronic properties of graphene. *Reviews of Modern Physics*. 2009;**81**:109-162
- [3] Stajic J. Hydrogen atom makes graphene magnetic. *Science*. 2016;**352**(6284):424
- [4] Avouris P, Chen ZH, Perebeinos V. Carbon-based electronics. *Nature Nanotechnology*. 2007;**2**:605-615
- [5] Dragoman M, Dragoman D. Graphene-based quantum electronics. *Progress in Quantum Electronics*. 2009;**33**:165-214
- [6] Castro Neto AH. The carbon new age. *Materials Today*. 2010;**13**:12-17
- [7] Garcia JC, de Lima DB, Assali LVC, Justo JF. Group IV graphene- and graphene-like nanosheets. *Journal of Physical Chemistry C*. 2011;**115**(27):13242-13246
- [8] Ashton M, Paul J, Sinnott SB, Hennig RG. Topology-scaling identification of layered solids and stable exfoliated 2D materials. *Physical Review Letters*. 2017;**118**:106101
- [9] MaterialsWeb.org–Databases of Structural, Electronic, and Thermodynamic data for 2D and 3D Materials
- [10] Graphene-Info Market Report. Graphene-info; June 2015
- [11] <https://www.wired.com/2010/10/graphene/>
- [12] Global Demand for Graphene after Commercial Production to be Enormous. AZONANO.com; 28 February 2014
- [13] Koppens FHL, Mueller T, Avouris P, Ferrari AC, Vitiello MS, Polini M. Photodetectors based on graphene, other two-dimensional materials and hybrid systems. *Nature Nanotechnology*. 2014;**9**:780-793
- [14] Fang H, Bechtel HA, Plis E, Martin MC, Krishna S, Yablonovitch E, Javey A. Quantum of optical absorption in two-dimensional semiconductors. *Proceeding National Academy Science*. 2013;**110**(29):11688-11691
- [15] <https://www.semiconductors.org/>
- [16] https://en.wikipedia.org/wiki/Integrated_circuit
- [17] Moore GE. Cramming more components onto integrated circuits. *Electronics Magazine*. 1965;**38**(8):4

- [18] Arden W, Brillouet M, Coge P, Graef M, Huizing B, Manhkopf R. More-than-Moore White Paper
- [19] Waldrop MM. The chips are down for Moore's law. *Nature*. 2016;**530**:144-147
- [20] https://en.wikipedia.org/wiki/Apples_mobile_application_processors
- [21] Huang JS, Jan YH. Environmental Engineering of Photonic and Electronic Reliabilities: From Technology and Energy Efficiency Perspectives. Saarbrücken, Germany: Scholars' Press; 2017
- [22] Campbell JC. Recent advances in avalanche photodiodes. *Journal of Lightwave Technology*. 2016;**34**(2):278-285
- [23] Huang JS, Chang HS, Jan YH, Chen HS, Ni CJ, Chou E. Temperature dependence study of mesa-type InGaAs/InAlAs avalanche photodiode characteristics. *Advances in OptoElectronics*. 2017:1-5. Article ID 2084621
- [24] Chen YH, Wun JM, Wu SL, Chao RL, Huang JS, Jan YH, Chen HS, Ni CJ, Chang HS, Chou E, Shi JW. Top-illuminated In_{0.52}Al_{0.48}As-based avalanche photodiode with dual charge layers for high-speed and low dark current performances. *IEEE Journal of Selected Topics in Quantum Electronics*. March/April, 2018;**24**(2):3800208
- [25] Nada M, Muramoto Y, Yokoyama H, Ishibashi T, Kodama S. InAlAs APD with high multiplied responsivity-bandwidth product (MR-bandwidth product) of 168 A/W·GHz for 25 Gbit/s high-speed operations. *Electronics Letters*. 2012;**48**(7):397-399
- [26] Huang M, Cai P, Li S, Wang L, Su T-I, Zhao L, Chen W, Hong C-Y, Pan D. Breakthrough of 25Gb/s Germanium on Silicon Avalanche Photodiode. *Optical Fiber Communications Conf., Technical Digest*, paper Tu2D.2, (OFC, Anaheim, CA, 2016)
- [27] Ishimura E, Yagyu E, Kaji MN, Ihara S, Yoshiara K, Aoyaji T, Tokuda Y, Ishikawa T. Degradation mode analysis on highly reliable guardring-free planar InAlAs avalanche photodiode. *Journal of Lightwave Technology*. 2007;**25**(12):3686-3693
- [28] Achouche M, Glastre G, Caillaud C, Lahrichi M, Chitoui M, Carpentier D. InGaAs communication photodiodes: From low- to high-power-level designs. *IEEE Photonics Journal*. 2010;**2**(3):460-468
- [29] Kim HS, Choi JH, Bang HM, Jee Y, Yun SW, Burm J, Kim MD, Choo AG. Dark current reduction in APD with BCB passivation. *Electronics Letters*. 2001;**37**(7):455-457
- [30] Takeshita T, Hirota Y, Ishibashi T, Muramoto Y, Ito T, Tohmori Y, Ito H. Degradation behavior of avalanche photodiodes with a mesa structure observed using a digital OBIC monitor. *IEEE Transactions on Electron Devices*. 2006;**53**(7):1567-1574
- [31] Watanabe I, Tsuji M, Hayashi M, Makita K, Taguchi K. Reliability of mesa-structure InAlGaAs-InAlAs superlattice avalanche photodiodes. *IEEE Photonics Technology Letters*. 1996;**8**(6):824-826

- [32] Smith GM, McIntosh KA, Donnelly JP, Funk JE, Mahoney LJ, Verghese S. Reliable InP-based Geiger-mode avalanche photodiode array. *Proceedings of SPIE*. 2009;**7320**:1-10
- [33] Pearsall TP. Impact ionization rates for electrons and holes in GaInAs. *Applied Physics Letters*. 1980;**36**:218-220
- [34] Oasaka F, Mikawa T. Excess noise design of InP/InGaAsP/InGaAs avalanche photodiodes. *IEEE Journal of Quantum Electronics*. 1986;**QE-22**:471-478
- [35] Neitzert HC, Cappa V, Crovato R. Influence of the Device Geometry and Inhomogeneity on the Electrostatic Discharge Sensitivity of InGaAs/InP Avalanche Photodiode. *EOS/ESD Symposium*. CA: Santa Clara; 1997
- [36] Nada M, Yoshimatsu T, Muramoto Y, Yokoyama H, Matsuzaki H. Design and performance of high-speed avalanche photodiodes for 100-Gb/s systems and beyond. *IEEE/OSA Journal of Lightwave Technology*. 2015;**33**(5):984-990
- [37] Ma CLF, Deen MJ, Tarof LE, Yu J. Modelling of breakdown voltage and its temperature dependence in SAGCM InP/InGaAs avalanche photodiodes. *IEEE International Electron Devices Meeting (IEDM, Dec., 1994, San Francisco, CA)*, pp. 22.5.1-22.5.4
- [38] Huang JS, Chang HS, Jan YH, Chen HS, Ni CJ, Chou E, Lee SK, Shi J-W. Highly Reliable, Cost-Effective and Temperature-Stable Top-Illuminated Avalanche Photodiode (APD) for 100G Inter-Datacenter ER4-Lite Applications Photoptics. Portugal: Funchal; 2018 in press
- [39] Huang JS, Chang HS, Jan YH. Reliability challenges of nanoscale avalanche photodiodes. *Open Access Journal of Photoenergy*. 2017;**1**(3):00015
- [40] Viswanathan CR. *Physical Principles of Semiconductor Devices*. UCLA: EE Class Note; 1993. p. 172-208
- [41] Hu C. *PN and Metal-semiconductor Junctions*. UC, Berkeley, EE Class Note, Chapter 4. 2009. pp. 89-156
- [42] Bendib T, Pancheri L, Dieffal F, Betta GFD. Impact of temperature and doping concentration on avalanche photodiode characteristics. *Proceed. World Congress Eng., vol.I, (WCE, July, 2014, London, UK)*, pp. 5-8
- [43] Massey DJ, David JPR, Rees GJ. Temperature dependence of impact ionization in sub-micronmeter silicon devices. *IEEE Transactions on Electron Devices*. 2006;**53**:2328-2334
- [44] Tyagi MS. Zener and avalanche breakdown in silicon alloyed p-n junctions. *Solid State Electronics*. 1968;**11**:99-128
- [45] Tan LLJ, Ong DSG, Ng JS, Tan CH, Jone SK, Qian Y, David JPR. Temperature dependence of avalanche breakdown in InP and InAlAs. *IEEE Journal of Quantum Electronics*. 2010;**46**(8):1153-1157
- [46] Ohnaka K, Kubo M, Shibata J. A low dark current InGaAs/InP p-i-n photodiode with covered mesa structure. *IEEE Transactions on Electron Devices*. 1987;**ED-34**(2):199-204

- [47] Fukuda M. Optical semiconductor devices. Chapter 4 Photodiodes. 1999. Wiley, New York, NY
- [48] Forrest SR, Leheny RF, Nahory RE, Pollack MA. $\text{In}_{0.53}\text{Ga}_{0.47}\text{As}$ photodiodes with dark current limited by generation-recombination and tunneling. *Applied Physics Letters*. 1980;**37**:322-324
- [49] Thomson JD, Summers HD, Snowton PM, Herrmann E, Blood P, Hopkinson M. Temperature dependence of the lasing wavelength of InGaAs quantum dot lasers. *Journal of Applied Physics*. 2001;**90**(9):4859-4861
- [50] Pearsall TP. $\text{Ga}_{0.47}\text{In}_{0.53}\text{As}$: A ternary semiconductor for photodetector applications. *IEEE Journal of Quantum Electronics*. 1980;**16**(7):709-720
- [51] Pearsall TP, Eaves L, Portal JC. Photoluminescence and impurity concentration in $\text{Ga}_x\text{In}_{1-x}\text{As}_y\text{P}_{1-y}$ alloys lattice-matched to InP. *Journal of Applied Physics*. 1983;**54**(2):1037-1047
- [52] Laird JS, Hirao T, Onoda S, Ohyama H, Kamiya T. Heavy-ion induced single-event transients in high-speed InP-InGaAs avalanche photodiodes. *IEEE Transactions on Nuclear Science*. 2003;**50**(6):2225-2232
- [53] Alpert A. High-Speed Jitter Testing of XFP Transceivers. Viavi White Paper; 2015
- [54] Generic reliability assurance requirements for optoelectronic devices used in telecommunication equipment. Telcordia, GR-468-CORE; 2004
- [55] Black JR. Electromigration failure modes in aluminum metallization for semiconductor devices. *Proceedings of the IEEE*. 1969;**57**(9):1587-1594
- [56] Huang JS. Temperature and current dependences of reliability degradation of buried heterostructure semiconductor lasers. *IEEE Transactions on Device and Materials Reliability*. 2005;**5**(1):150-154
- [57] Huang JS, Nguyen T, Hsin W, Aeby I, Ceballo R, Krogen J. Reliability of etch-mesa buried-heterostructure semiconductor lasers. *IEEE Transactions on Device and Materials Reliability*. 2005;**5**(4):665-674
- [58] Watanabe I, Tsuji M, Hayashi M, Makita K, Taguchi K. Reliability of mesa-structure InAlGaAs-InAlAs superlattice avalanche photodiodes. *IEEE Photonics Technology Letters*. 1996;**8**(6):824-826
- [59] Huang JS. Design-in reliability of modern wavelength-division multiplex (WDM) distributed feedback (DFB) lasers. *Applied Physics Research*. 2012;**4**(2):15-28
- [60] Bandi UR, Dasaka M, Kumar PK. Design in Reliability for Communication Designs. 43rd ACM/IEEE Design Automation Conference (San Francisco, CA, 2006)
- [61] Fukuda M. Reliability and Degradation of Semiconductor Lasers and LEDs. Artech House: Norwood, MA; 1994

- [62] Oates AS, Lin MH. Electromigration failure distributions of cu/low-k dual-damascene vias: Impact of the critical current density and a new reliability extrapolation methodology. *IEEE Transactions on Device and Materials Reliability*. 2009;**9**(2):244-254
- [63] Huang JS, Shofner TL, Zhao J. Direct observation of void morphology in step-like electromigration resistance behavior and its correlation with critical current density. *Journal of Applied Physics*. 2001;**89**(4):2130-2133
- [64] Efremov AA, Bochkareva NI, Gorbunov RI, Lavrinovich DA, Tarkhin YTRDV, Shreter YG. Effect of the joule heating on the quantum efficiency and choice of thermal conditions for high-power blue InGaN/GaN LEDs. *Physics of Semiconductor Devices*. 2006;**40**(5):605-610
- [65] Wachutka GK. Rigorous thermodynamic treatment of heat generation and conduction in semiconductor device modeling. *IEEE Transactions on Computer-Aided Design of Integrated Circuits and Systems*. 1990;**9**(11):1141-1149
- [66] Huang JS. "Reliability of Optoelectronics", Chapter 6 in *Reliability Characterisation of Electrical and Electronic Systems*. Cambridge, UK: Woodhead Publishing; 2015
- [67] Tu KN, Yeh CC, Liu CY, Chen C. Effect of current crowding on vacancy diffusion and void formation in electromigration. *Applied Physics Letters*. 2000;**76**(8):988-990
- [68] Yeh ECC, Choi WJ, Tu KN. Current crowding-induced electromigration in flip chip solder joints. *Applied Physics Letters*. 2001;**80**(4):580-282
- [69] Huang JS, Yeh ECC, Zhang ZB, Tu KN. The effect of contact resistance on current crowding and electromigration in ULSI interconnects. *Materials Chemistry and Physics*. 2002;**77**(2):377-383
- [70] Ma Y, Zhang Y, Gu Y, Chen X, Shi Y, Ji W, Xi S, Du B, Li X, Tang H, Li Y, Fang J. Impact of etching on the surface leakage generation in mesa-type InGaAs/InAlAs avalanche photodetectors. *Optics Express*. 2016;**24**(7):7823-7834
- [71] Sudo H, Suzuki M. Surface degradation mechanism of InP/InGaAs APD. *Journal of Lightwave Technology*. 1988;**6**(10):1496-1501
- [72] Huang JS, Jan YH, Chen HS, Chang HS, Ni CJ, Chou E. Predictive reliability model of 10G/25G mesa-type avalanche photodiode degradation. *Applied Physics Research*. 2016;**8**(3):66-74
- [73] Huang JS, Jan YH, Chang HS, Chang J, Chang R, Liu G, Ren D, Chou E. ESD polarity effect study of monolithic, integrated DFB-EAM EML for 100/400G optical networks. *CLEO-PR* (Singapore, July31-Aug.4, 2017), Paper#1018
- [74] Saleh MA, Hayat MM, Kwon OH, Holmes AL, Campbell JC, Saleh BEA, Teich MC. Breakdown voltage in thin III-V avalanche photodiodes. *Applied Physics Letters*. 2001;**79**(24):4037-4039

- [75] Huang JS, Yu-Heng J. Interconnected analogy and resemblance: from classical music to modern semiconductor technology. *International Journal of Electronics and Electrical Engineering*. 2016;**5**(2):1-8
- [76] Huang JS, Jan YH. A complexity science study: Effect of critical current density on semiconductor laser diodes and integrated circuits. *Journal of Systemics, Cybernetics Informatics*. 2017;**15**(1):77-83

